Mathematical Modeling and Multiobjective Optimization of Negative-Coupled Inductor in Multiphase Interleaved DC–DC Converter

Ze Liu, Guohua Zhou, *Senior Member, IEEE*, Yingjie He, and Nengmou Xu, *Student Member, IEEE*

***Abstract*—To optimize the converter efficiency, footprint and volume of magnetic devices simultaneously, this article proposes a mathematical modeling and multiobjective optimization method based on multiphase negative-coupled inductor (NCI) in interleaved dc–dc converter, and elaborates on the specific details by taking interleaved buck converter (IBC) and four-phase NCI as an example. First, flux cancellation is employed to design a four-phase NCI without core center column. Next, comprehensive mathematical models of NCI are established considering essential parameters. Subsequently, the Pareto Front of the objective function and converter efficiency constraint is identified through the multiobjective optimization based on the modeling results, enabling tradeoff for optimal parameters selection of NCI. Finally, an experimental prototype of 300 W demonstrates that compared to separate inductors, NCI reduces footprint and volume by 41.31% and 60.90%, respectively, while achieving the magnetic device power density of 7376 W/in^3, the 1.45% improvement of rated efficiency and better transient performance of IBC.**

***Index Terms*—Four-phase negative-coupled inductor (NCI), interleaved buck converter (IBC), mathematical modeling, multiobjective optimization.**

I. Introduction

THE rapid development of industries such as aerospace, military equipment, electric vehicles, and green data centers has imposed new demands on the high efficiency, high power density, light weight, and miniaturization of intermediate-stage low-power nonisolated switching power supplies [1], [2], [3]. To minimize output current ripple, intermediate-stage converters frequently employ the multiphase interleaved dc–dc converter, such as multiphase interleaved buck converter (IBC), which is exhibited in Fig. 1.

Received 5 May 2025; revised 24 September 2025 and 17 November 2025; accepted 5 December 2025. Date of publication 10 December 2025; date of current version 25 February 2026. This work was supported in part by the National Natural Science Foundation of China under Grant 62271417, and in part by the Sichuan Provincial Engineering Research Center of High Efficiency Power Converter Technology under Grant 2023-02. Recommended for publication by Associate Editor Y. Qin. *(Corresponding author: Guohua Zhou.)*

The authors are with the Key Laboratory of Magnetic Suspension Technology and Maglev Vehicle, Ministry of Education, Southwest Jiaotong University, Chengdu 611756, China, and also with the School of Electrical Engineering, Southwest Jiaotong University, Chengdu 611756, China (e-mail: smithereens@my.swjtu.edu.cn; eeghzhou@swjtu.edu.cn; hh_123@my.swjtu.edu.cn; nengmouxu@my.swjtu.edu.cn).

Color versions of one or more figures in this article are available at https://doi.org/10.1109/TPEL.2025.3642890.

Digital Object Identifier 10.1109/TPEL.2025.3642890

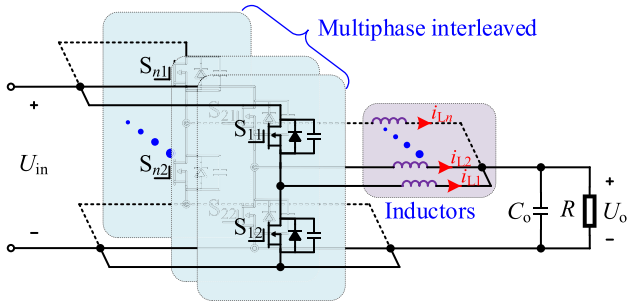

Fig. 1. Multiphase IBC.

However, magnetic devices typically account for over 30% of the power supply volume and are critical factors influencing its power density and output characteristics [4], [5]. To further decrease the footprint, volume, and loss of magnetic devices while enhancing the efficiency of power supply, magnetic integration serves as an effective solution [6], [7], [8].

Integrating multiple separate inductors (SI) can effectively enhance the efficiency and power density of converters [9], [10]. Segmented windings enable the integration of multiple SI onto a single magnetic core, thereby reducing the volume and weight of magnetic device as well as the converter loss [11]. However, this method employs a decoupled integration approach, which limits volume and weight reduction compared to SI, because phases hardly share the magnetic flux paths with each other. Positive-coupling is usually used to achieve specific converter functions, such as soft-switching for losses reduction and zero output current ripple [12], [13]. However, positive-coupling is rarely applied in multiphase interleaved dc–dc converters, because the currents of phases will cause the fluxes to superimpose and enhance each other in the core, which often leads to the increase in phase current ripple and core saturation at high load conditions. The negative-coupling method effectively mitigates the common-mode noise of the converter by constructing a specific equivalent circuit [14], [15], [16], [17]. And experimental results demonstrate that besides reducing noise, negative-coupled inductor (NCI) significantly reduces magnetic devices volume by flux cancellation, enhances converter power density and electromagnetic compatibility, and improves converter efficiency and phases current sharing. Furthermore, the NCI also can improve the transient performance of converter [18]. However, the NCI cores in [14], [15], [16], [17],

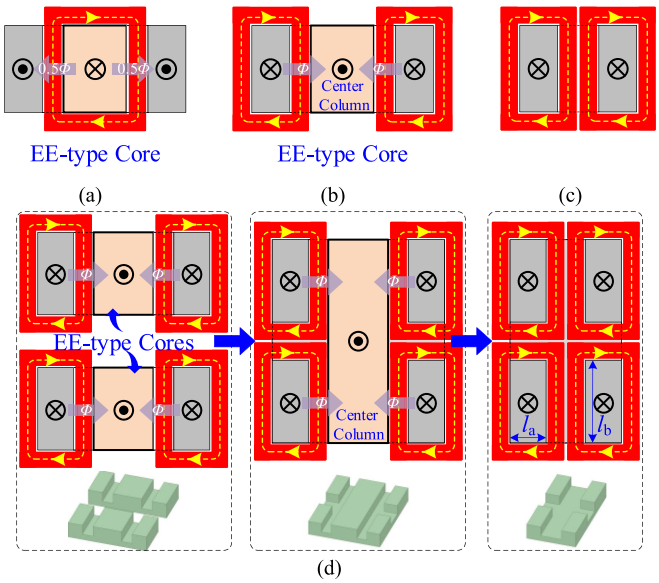

Fig. 2. Deduction process of four-phase NCI. (a) Traditional single-winding inductor with an EE-type core. (b) Two-phase coupled inductor with an EE-type core. (c) Two-phase NCI without center column. (d) Process of deducing four-phase NCI without center column.

and [18] are modified based on traditional EE-type cores, the volume of cores can be further optimized due to the existence of center columns.

For converters utilizing printed circuit board (PCB) based magnetic devices, the design of planar integrated magnetic devices is becoming increasingly standardized and process-oriented, the design process typically considers various factors, such as footprint and volume [19]. During the multiobjective optimization design for coupled inductor, multiple parameters are commonly used to model and optimize the inductor loss, thereby obtaining parameter values that meet the design requirements [20], [21]. However, this approach does not account for the effects of switching frequency and coupling coefficient on loss, and due to the lack of key constraints, the computational complexity of the optimization process becomes relatively high. Ulteriorly, by adding converter efficiency as a constraint, the Pareto Front of the coupled inductor volume and converter efficiency is studied [22], [23], [24]. Nevertheless, the influence of winding turns on winding loss is neglected, leading to reduced accuracy of the loss model at high frequency, besides, focusing solely on volume of magnetic devices cannot satisfy modern design requirements, and as the number of iteration parameters increases, the curve of Pareto Front will become unsmooth, seriously affecting the subsequent parameter tradeoff. Overall, due to the limitations of variables in loss model and deficiencies in optimization process, the aforementioned approaches fail to provide adequate guidance for modeling and optimization of NCI.

In order to minimize the footprint and volume of the core to the greatest extent while avoiding core saturation, this article adopts the NCI structure for design. To achieve the simultaneous optimization of converter efficiency, footprint, and volume of magnetic devices, this article proposes a mathematical modeling and multiobjective optimization method for the multiphase NCI in interleaved dc–dc converter, with the IBC and a four-phase NCI serving as a specific example. The main contributions of this work are summarized as follows:

1) A multiphase NCI without core center column is deduced systematically by flux cancellation, and a four-phase NCI with high power density is designed as a specific example.
2) The comprehensive mathematical models for the four-phase NCI and IBC are proposed, accurately representing their characteristics using the most basic variables.
3) A modeling-based multiobjective optimization method for four-phase NCI and IBC is proposed. Normalization and weighting ensure consistent optimization of footprint and volume, while dividing the Pareto Front by the value of winding turns makes the parameter tradeoff more intuitive.

The rest of this article is organized as follows. Section II details the derivation process of the four-phase NCI. The mathematical modeling of NCI is discussed in Section III. The multiobjective optimization method and the corresponding results are elaborated in Section IV. Section V provides the experimental results. Finally, Section VI concludes this article.

II. NCI Structure Deduction

For the multiphase IBC in Fig. 1, a four-phase configuration is taken as an example for the mathematical modeling and multiobjective optimization of NCI based on planar PCB.

It should be emphasized that the reason for selecting the IBC as an example is to demonstrate the practicability of the designed NCI, proposed mathematical modeling and multiobjective optimization methods in this article. In fact, the content presented in this article is not only applicable to the IBC, but also applicable to other multiphase interleaved converters that satisfy the following conditions.

1) The converter operates in continuous current mode, and the inductor current comprises both dc and ac components before coupling.
2) The amplitudes of the current in each phase are equal, their directions are consistent, only the phase differences exist.

Identifying the NCI core shape is a critical step in magnetic device design and serves as a fundamental prerequisite for effective modeling and optimization. The evolution process of the four-phase NCI core is presented in Fig. 2. Fig. 2(a) depicts a traditional single-winding inductor with an EE-type core. By winding two separate windings on the two side columns of the core, a two-phase coupled inductor can be formed, as illustrated in Fig. 2(b). For the coupled inductor in Fig. 2(b), due to negative-coupling, the coupling coefficient between the two phases is relatively big, the change in air gap of the center column has no significant impact on it. Therefore, as stated in Fig. 2(c), a two-phase NCI without center column is formed by removing the center column and bringing two side columns closer. The coupling coefficient is adjusted by changing the air gap of the two side columns.

Furthermore, by integrating two two-phase coupled inductors depicted in Fig. 2(b), extending the upper and lower cover plates and the core center column, a four-phase coupled inductor can be formed. Subsequently, by removing the center column, a four-phase NCI without center column can be obtained, the process

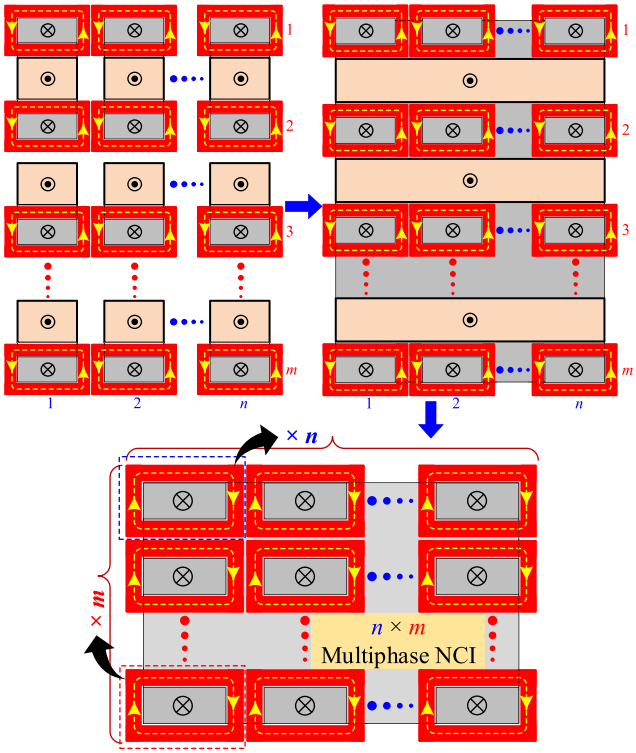

Fig. 3. Process of deducing $n \times m$ multiphase NCI.

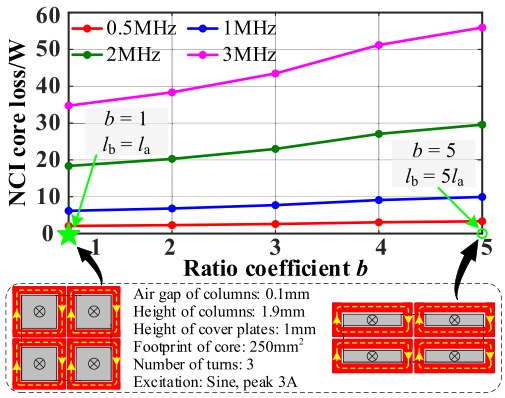

Fig. 4. Four-phase NCI core loss under different ratio coefficient b.

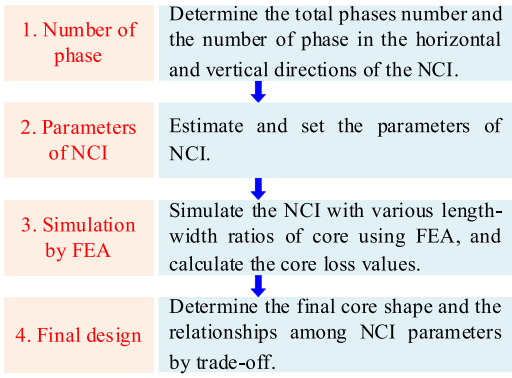

Fig. 5. General derivation flow of the multiphase NCI core structure.

is illustrated in Fig. 2(d). Compared to SI, this modification not only effectively exploits the dc flux cancellation to achieve a low-height core design, but also reduces the core magnetic reluctance, ensuring more uniform flux distribution [25].

Similar to the four-phase NCI derivation, multiple two-phase coupled inductors using EE-type core are arranged horizontally, while multiple units consist of center and side columns are added vertically. Extending cover plates and center columns achieves negative-coupling among multiple phases. Since air gap variations in the center columns barely affect phases coupling coefficients, an $n \times m$ multiphase NCI can be obtained by removing center columns and bringing phases closer. The process is shown in Fig. 3. For multiphase NCI, mutual-inductances are more complex, requiring specific analysis for each phase. As flux cancellation degrees of phases vary, not all winding current are the same, therefore, parameters of each phase should be calculated according to the specific requirements. Moreover, the high-order harmonics brought by multiphase coupling cannot be ignored.

In fact, the mathematical modeling and multiobjective optimization method proposed in this article are not only applicable to the matrix NCI but also can be extended to other configurations and geometries of planar NCI, such as circular and polygonal structures. However, to enhance the utilization efficiency of the NCI core and present the universality of the proposed method, this study focuses exclusively on the matrix NCI, and takes four-phase NCI as an example.

As shown in Fig. 2(d), the shape of four-phase NCI should be further optimized. The aspect ratio of the core column is defined as b ($l_b = b \times l_a$). Finite element analysis (FEA) is used to simulate the NCI under various b. The parameters of the NCI and core losses are shown in Fig. 4.

As shown in Fig. 4, when b equals 1, core losses are minimum at all frequencies. The increase of b leads to more core loss. This is because as b increases, the uniformity of flux distribution within the core decreases, and the complexity of mutual-inductances increases, which aggravates the deformation of winding current and generates more high-order harmonics. All these factors result in the increase of NCI core loss. Therefore, a design with a square cross-section for the core column is adopted, with its side length is set as l_e. Furthermore, to enhance the magnetic shielding effect of the core, minimize interference with surrounding electronic components, and improve heat dissipation, the cover plates of the NCI core are extended to fully cover the windings [26].

By combining the design of the multiphase NCI core structure and focusing on the core column with rectangle cross-section, the general derivation process for the shape of multiphase NCI core can be obtained, the flowchart is shown in Fig. 5. It should be noted that the parameters are set merely for simulating the NCI core loss and do not need to be set according to the actual NCI core and current excitation. The derivation of the four-phase NCI

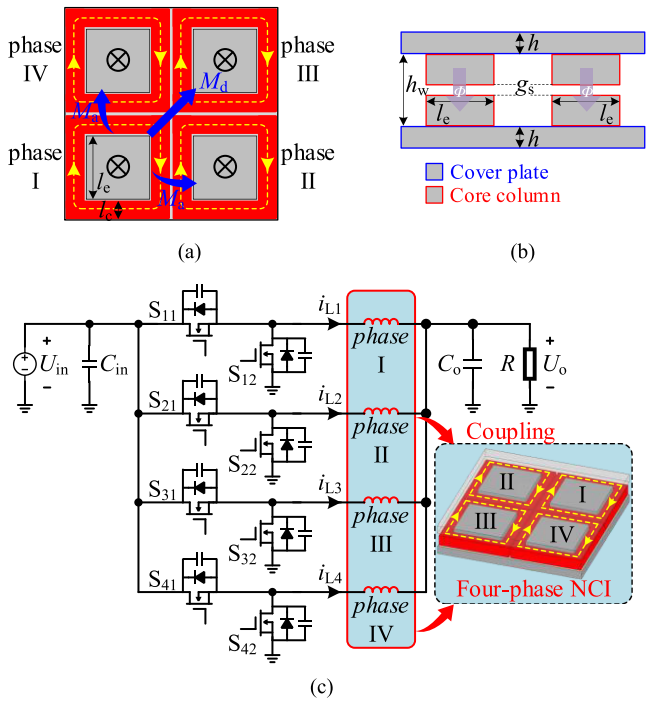

Fig. 6. Four-phase NCI presented in this article. (a) Platform view and winding phase sequence of NCI. (b) Front view and key parameters of NCI core. (c) Four-phase IBC utilizing NCI.

core shape can be regarded as a specific instance of the process shown in Fig. 5.

The abovementioned process results in the final four-phase NCI in this work, as illustrated in Fig. 6(a), with the winding sequence arranged in a counter-clockwise direction. The front view and key parameters of the four-phase NCI are depicted in Fig. 6(b). Fig. 6(c) presents the schematic diagram of the four-phase IBC utilizing NCI.

For design simplicity, the columns of the NCI core in Fig. 6(a) are designed to have uniform height. In four-phase NCI, the mutual-inductances between adjacent phases and diagonal phases are different, represented by M_a and M_d, respectively. Additionally, k_a and k_d are employed to represent the coupling coefficients of the adjacent and diagonal phases. The relationships between k_a, k_d and M_a, M_d can be expressed as

$$M_a = k_a L, M_d = k_d L \tag{1}$$

where L presents the self-inductance of per NCI phase.

As for Fig. 6, the footprint FP and volume V_e of the four-phase NCI can be derived as

$$\begin{cases} FP = (2l_e + 4l_c)^2 \\ V_e = (h_w + 2h)FP = (h_w + 2h)(2l_e + 4l_c)^2 \end{cases} \tag{2}$$

where h and l_c represent the thickness of each cover plate and the width of winding turns, as illustrated in Fig. 6. Since NCI utilize PCB winding, and four-phase negative-coupling effectively reduces dc flux in two cover plates, the core window height h_w is set to 2 mm for design simplicity.

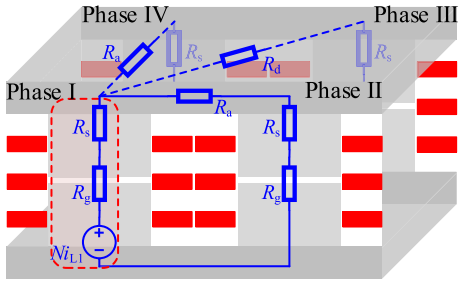

Fig. 7. Magnetic reluctance model of four-phase NCI.

III. Mathematical Modeling of Four-Phase NCI

After determining the shape of four-phase NCI core, the mathematical modeling processes of four-phase NCI are conducted to establish a practical foundation for multiobjective optimization. These models contain the magnetic reluctance model, electrical characteristics, and loss model. All expressions are formulated based on the side length of the core column, air gap, switching frequency, and winding turns. The three modeling parts can be regarded as the processes of numerically representing the characteristics of NCI and IBC using several basic parameters from different dimensions.

A. Magnetic Reluctance Model

The magnetic reluctance model for the first phase of the four-phase NCI is illustrated in Fig. 7. To simplify the design process while ensuring the consistency of four phases parameters, the number of winding turns N is uniformly set to the same value.

In Fig. 7, i_{L1} represents the current of the first phase, R_s denotes the magnetic reluctance of the core column, R_g indicates the magnetic reluctance of air gap g_s, R_a and R_d correspond to the magnetic reluctances of the cover plates for the adjacent and diagonal phases, respectively. All above variables can be expressed as follows:

$$\begin{cases} R_s = \frac{h_w - g_s}{{l_e}^2 \mu_r}, R_g = \frac{g_s}{{l_e}^2 \mu_0} \\ R_d = \sqrt{2} R_a = 2\sqrt{2} \frac{l_e + 2l_c}{l_e h \mu_r} \end{cases} \tag{3}$$

where μ_0 and μ_r represent the permeability of the vacuo and the relative permeability of the magnetic material, respectively.

Furthermore, by applying the equivalent magnetic circuit method, self-inductance L and mutual-inductances M_a and M_d can be derived. Their respective expressions are as follows:

$$\begin{cases} L = \frac{N^2}{R_s + R_g + (R_d + R_s + R_g) \| [(R_a + R_s + R_g)/2]} \\ M_a = \frac{M[(R_d + R_s + R_g) \| (R_a + R_s + R_g)]}{(R_d + R_s + R_g) \| (R_a + R_s + R_g) + R_a + R_s + R_g} \\ M_d = \frac{M(R_a + R_s + R_g)/2}{(R_a + R_s + R_g)/2 + R_d + R_s + R_g} \end{cases} \tag{4}$$

where M is an intermediate variable, its expression is

$$M = -L \frac{(R_d + R_s) \| [(R_a + R_s)/2] + R_s}{(R_d + R_s) \| [(R_a + R_s)/2] + R_s + 4R_g/3}. \tag{5}$$

FEA is employed to validate (4) under the condition of $N = 5$, $h = 1$ mm, and varying l_e and g_s within specified ranges.

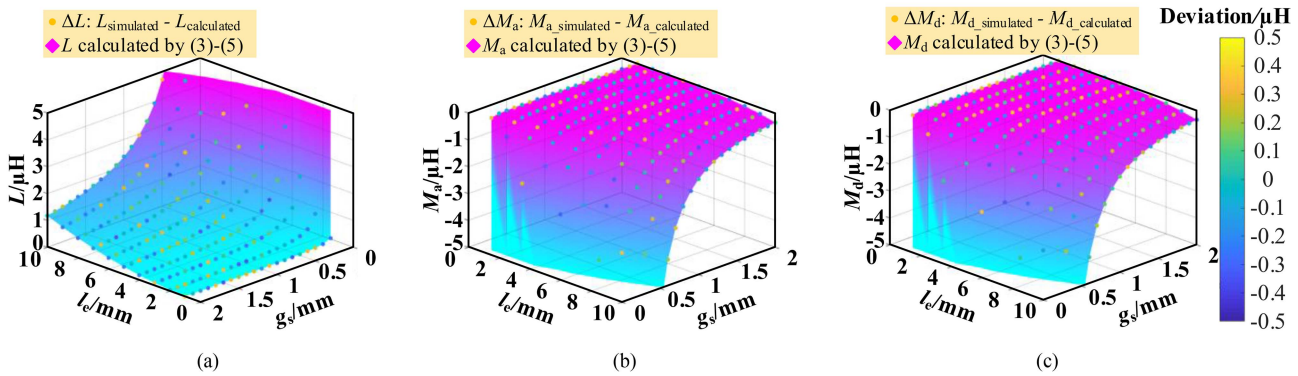

Fig. 8. Simulation verification of the expressions related to four-phase NCI. (a) Verification of L. (b) Verification of M_{a}. (c) Verification of M_{d}.

The results are shown in Fig. 8, where the surfaces represent the theoretical values calculated by (3)–(5), and the dots indicate the deviations between simulation and theoretical results. It can be observed that the deviations remain within 0.5 μH across the parameter variation ranges, confirming the accuracy of (3)–(5) and providing a substantial theoretical foundation for the subsequent optimization process.

B. Electrical Characteristics

The four-phase negative-coupling in IBC splits the winding current into 8 segments per switching period. In four-phase IBC with NCI, as illustrated in Fig. 6, the current phases increment sequentially by 90°. This results in different trends of winding current variations within different duty cycle ranges, as depicted in Fig. 9.

In Fig. 9, taking the first phase as an example, the winding current is segmented into 8 modes over t_0–t_8, each mode corresponding to an equivalent modal inductance $L_{\mathrm{mod}\,j}$ (j = 1, 2, …8). Because the duty cycle varies, the winding current exhibits different modal characteristics, leading to different expressions for the equivalent steady-state inductance L_{ss} within different duty cycle ranges. Equation (6) presents the formula for calculating L_{ss} when $0.25 \le D < 0.5$, as illustrated in Fig. 9(b). Similarly, the corresponding expressions of L_{ss} for other duty cycle ranges are summarized in Table I

$$L_{\mathrm{ss}} = \frac{D}{\frac{D-1/4}{L_{\mathrm{mod}\,1}} + \frac{1/2-D}{L_{\mathrm{mod}\,2}} + \frac{D-1/4}{L_{\mathrm{mod}\,3}}}, D \in [0.25, 0.5). \quad (6)$$

The winding current ripple Δi_{Lss} of the IBC using NCI within each switching period can be calculated as follows:

$$\Delta i_{\mathrm{Lss}} = \frac{U_{\mathrm{in}} - U_{\mathrm{o}}}{L_{\mathrm{ss}} f_{\mathrm{s}}} D \quad (7)$$

where U_{in} and U_{o} represent the input and output voltages, respectively, while f_{s} denotes the switching frequency.

Assuming the inductance before coupling is L, under identical operating conditions, the comparison of winding current ripples after and before negative-coupling reveals that, based on Table I and (7), the ratio is a function regarding to L, M_{a}, M_{d}, and D. Consequently, the ratio of k_{a} and k_{d} is defined as g ($k_{\mathrm{a}} = g \times k_{\mathrm{d}}$). Fig. 10 illustrates the ratios of winding current ripples after and before negative-coupling under varying D and k_{d} when g equals 1.1 and 1.5.

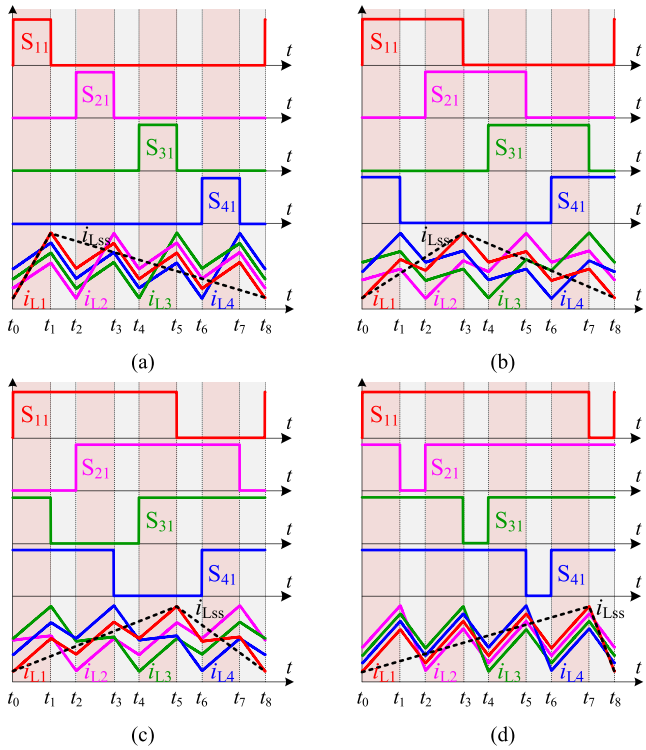

Fig. 9. Winding current of four-phase NCI under different duty cycle. (a) $0 \le D < 0.25$. (b) $0.25 \le D < 0.5$. (c) $0.5 \le D < 0.75$. (d) $0.75 \le D < 1$.

As shown in Fig. 10, the ratios of the winding current ripples after and before negative-coupling is divided into four regions based on different duty cycle ranges, which is consistent with the description of L_{ss} in Table I. Furthermore, it can be observed that within specific ranges of D and coupling coefficient, negative-coupling reduces the winding current, with the most significant effect occurring at the boundary values of D in four ranges. Additionally, it can also be concluded that as the coupling coefficient increases, the winding current ripple decreases.

In addition, Fig. 10 can also illustrate the ratio of inductance values before and after coupling, L/L_{ss}, under various duty cycles

TABLE I
EXPRESSIONS FOR L_{SS} ACROSS VARIOUS DUTY CYCLE RANGES

Duty cycle	Expression of L_{ss}
$0\le D<0.25$	$\frac{(D-1)(L-M_d)(L^2-4M_a^2+2LM_d+M_d^2)}{(D-1)L^2+2M_a^2+2DM_aM_d-DM_d^2-L(2DM_a+M_d)}$
$0.25\le D<0.5$	$\frac{2(D-1)D(L-M_d)(L-2M_a+M_d)(L+2M_a+M_d)}{M_a(M_d-L)+2D^2(L-M_d)(L-2M_a+M_d)-2Dx}$, $x=(L^2+L(M_d-2M_a)+2M_a(M_d-M_a))$
$0.5\le D<0.75$	$\frac{2(D-1)D(L-M_d)(L-2M_a+M_d)(L+2M_a+M_d)}{2L^2(D^2-D)+M_a(M_d-L)(4D^2-4D+1)+y}$, $y=(4M_a^2-2LM_d)(1-D)-2M_d^2(D^2-2D+1)$
$0.75\le D<1$	$\frac{D(L-M_d)(L^2-4M_a^2+2LM_d+M_d^2)}{M_d^2-2M_a^2-2M_aM_d+L(2M_a+M_d)+z}$, $z=D(L-M_d)(L-2M_a+M_d)$

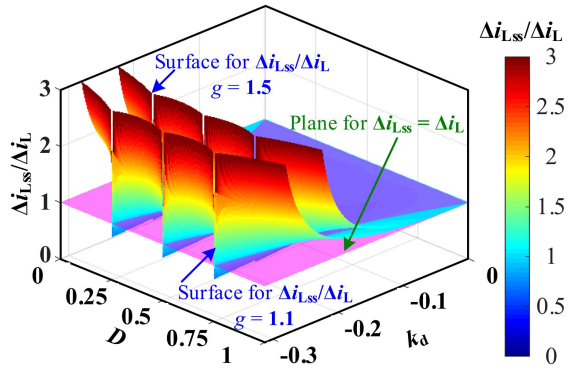

Fig. 10. Ratios of winding current ripples after and before negative-coupling.

and coupling coefficients while ensuring the winding current ripple remains constant.

C. Power Loss Model

When converter operates at high frequency, the magnetic flux density must remain within the characteristic range of the magnetic material. In addition, magnetic flux density is a critical factor influencing core loss. Consequently, before establishing the loss model, it is essential to analyze both the magnetic flux and flux density of four-phase NCI.

Based on Faraday's law of electromagnetic induction, the expressions for the dc flux Φ_{sdc} and the amplitude of ac flux $\Delta\Phi_s$ in four NCI core columns are as follows:

$$\begin{cases}\Phi_{sdc}=\frac{I_L L_{ss}}{N}\\ \Delta\Phi_s=\frac{U_{in}(1-D)D}{Nf_s}\end{cases} \tag{8}$$

where I_L denotes the average value of the single-phase winding current.

According to (8), the maximum flux density B_{max} of the core column can be derived as follows:

$$B_{max}=\frac{2\Phi_{sdc}+\Delta\Phi_s}{2l_e^2}=\frac{2I_L L_{ss}f_s+U_{in}(1-D)D}{2Nf_s l_e^2}. \tag{9}$$

Due to the negative-coupling, the dc fluxes of the four phases are canceled out within the cover plates, while the amplitude of ac flux in the cover plates does not exceed its value in any single core column. To maintain consistency between the maximum flux density in the cover plates and core columns with a certain margin, the thickness h of each cover plate is determined by the amplitude of the ac flux density in single core column. The expression of h is given as

$$h=\frac{\Delta\Phi_s}{4l_e B_{max}}=\frac{U_{in}l_e(1-D)D}{4f_s I_L L_{ss}+2U_{in}(1-D)D}. \tag{10}$$

The core loss of NCI can be calculated using the modified generalized Steinmetz equation, which can be presented as

$$\begin{cases}P_e=P_s+P_b\\ P_s=\frac{4l_e^2(h_w-g_s)k_f B_{ac}^{\beta}f_s^{\alpha-1}}{4^{-\alpha}(1+\beta)(1+\beta+\alpha)}\\ P_b=\frac{2(2l_e+4l_c)^2hk_f B_{max}^{\beta}f_s^{\alpha-1}}{4^{-\alpha}(1+\beta)(1+\beta+\alpha)}\end{cases} \tag{11}$$

where k_f, α, and β represent the characteristic properties of magnetic material, B_{ac} denotes the amplitude of the ac flux density in the NCI core column, and P_s and P_b correspond to the losses in the core columns and cover plates, respectively.

The winding loss of four-phase NCI is expressed in (12), where P_{Cu_dc} and P_{Cu_ac} denotes the four-phase winding dc and ac losses, respectively, and P_{Cu_ac} is obtained from FEA. To reduce the winding current density, the winding width l_c is set to 1.5 mm. Additionally, each turn of the winding is configured as two parallel layers, with a copper thickness of 3oz per layer, resulting in a total thickness h_c of 6oz

$$\begin{cases}P_{Cu}=P_{Cu\_dc}+P_{Cu\_ac}\\ P_{Cu\_dc}=4I_L^2R_{dc}=4I_L^2\rho\frac{4(l_e+l_c)N}{h_c l_c}.\end{cases} \tag{12}$$

Each converter phase includes two MOSFETS operating complementarily. The total MOSFET loss (P_{mos}) in IBC can be given in (13). The losses of MOSFET mainly comprise turn-ON loss (P_{ON}), turn-OFF loss (P_{OFF}), and conduction loss (P_{ds}). Where R_{ON} and R_{OFF} represent the ON-state and OFF-state resistances, respectively. Q_{gs} and Q_{gd} denote the gate-source and gate-drain charges of MOSFET. V_{th} and V_c correspond to the threshold and Miller-platform voltage of MOSFET

$$\begin{cases}P_{mos}=4(P_{on}+P_{off}+P_{ds})\\ P_{ds}=I_L^2R_{ds}\\ P_{on}=R_{on}I_L U_{in}f_s(\frac{2Q_{gs}}{V_{th}+V_c}+\frac{Q_{gd}}{V_c})\\ P_{off}=R_{off}I_L U_{in}f_s(\frac{2Q_{gs}}{V_{th}+V_c}+\frac{Q_{gd}}{V_c}).\end{cases} \tag{13}$$

Based on (11)–(13), the rated efficiency η of four-phase IBC utilizing NCI can be expressed as

$$\eta=\frac{P_o}{P_o+P_e+P_{Cu}+P_{mos}}. \tag{14}$$

All aforementioned analysis and modeling methods are also applicable to the multiphase NCI shown in Fig. 3 and other

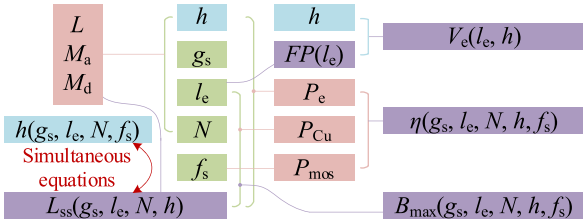

Fig. 11. Relationships among various variables.

dc–dc converters, excepting that certain steps need to be adjusted according to the specific number of phases.

By rearranging (2), (4), (9), (14), and Table I, the relationships among all abovementioned variables are illustrated in Fig. 11. L_{ss} and h are mutually dependent and satisfy an implicit function. By decoupling these two variables using (10) and Table I, it can be derived that h is a function of l_e, g_s, N, and f_s.

IV. Multiobjective Optimization of NCI

In the design of planar magnetic devices on PCB, it is essential to comprehensively consider crucial parameters such as the volume and footprint of the magnetic devices, the efficiency of the converter, and the saturation flux density of the magnetic core.

In this article, the volume and footprint of four-phase NCI are normalized and weighted as the objective function. Based on the modeling results, by continuously adjusting the efficiency constraint, the Pareto Front of efficiency constraint and objective function is derived. Finally, optimal parameters are selected based on practical tradeoff to achieve a balanced optimization among IBC efficiency, NCI volume and footprint, thereby ensuring the practical significance of the parameter selection.

A. Process of Multiobjective Optimization

The material of NCI core employed in this article is CETC9R53. This material exhibits a saturation flux density of 0.45 T at an ambient temperature of 25 °C. To avoid saturation of the NCI core, the flux density limit $B_{\lim}$ is set to 0.35 T.

By analyzing (2), (9), and (14), it is evident that optimizing NCI in this article includes setting the NCI footprint and volume as the optimization objectives, with IBC efficiency, flux density, and value of L_{ss} serving as constraint conditions. Given the different numerical ranges and units of the footprint and volume, the minimum-maximum normalization method presented in (15) can be employed to linearly map the two function values into the range of [0, 1]. The normalization ensures the optimization consistency of the footprint and volume of NCI

$$\begin{cases} \omega_{\mathrm{FP}} = \frac{FP - FP_{\min}}{FP_{\max} - FP_{\min}} \\ \omega_{\mathrm{Ve}} = \frac{V_e - V_{e\_\min}}{V_{e\_\max} - V_{e\_\min}} \end{cases} \tag{15}$$

where ω_{FP} and ω_{Ve} indicate the normalized values of the NCI footprint FP and volume V_e, respectively. Across all parameter variations, $FP_{\min}$ and $FP_{\max}$ represent the minimum and maximum of FP, while $V_{e\_\min}$ and $V_{e\_\max}$ correspond to the minimum and maximum of V_e.

TABLE II
Parameters of Four-Phase IBC

Description	Parameter	Value
Input voltage	U_{in}/V	28
Output voltage	U_o/V	12
Rated output current	I_o/A	25
Reference of L_{ss}, separate inductor	L_{sep}/μH	2.2
Minimum power density limit of NCI	\	5000 W/in^3
Minimum footprint of NCI	FP_{min}/mm^2	64
Maximun footprint of NCI	FP_{max}/mm^2	676
Minimum volume of NCI	V_{e_min}/mm^3	129.076
Maximum volume of NCI	V_{e_max}/mm^3	7261.05

TABLE III
Iteration and Increment of Parameters

Parameter	Iteration range	Increment
l_e/mm	1–10	0.1
N	2–6	1
g_s/mm	0–2	0.01
f_s/MHz	0.1–5	0.1
$\eta_{\lim}$	90%–100%	0.1%

To ensure the multiobjective optimization results are practically meaningful, the relevant parameters of the four-phase IBC are presented in Table II. For integrated magnetic device in IBC applications, a key designing principle is to maintain identical load characteristics when using either NCI or SI. Consequently, the design value of L_{ss} for NCI should be close with the value L_{sep} of SI.

In process of parameter iteration, the optimization function for NCI under efficiency constraint during the j_{th} iteration can be expressed as (16) and (17). Where ω_{FP} and ω_{Ve} represent the normalized values of the NCI footprint and volume. $\Delta\eta$ denotes the efficiency constraint increment. B_m corresponds to the maximum flux density of the NCI core. L_{ss} refers to the calculated equivalent steady-state inductance

$$\min(\omega_{\mathrm{FP}\_j} + \omega_{\mathrm{Ve}\_j}) \tag{16}$$

$$\text{s.t.} \begin{cases} \eta_{\lim\_j} \geq \eta_{\lim\_j-1} + \Delta\eta \\ B_{m\_j} \leq B_{\lim} \\ |L_{ss\_j} - L_{sep}| \leq 0.1 L_{sep}. \end{cases} \tag{17}$$

As shown by the above functions and Fig. 11, the designed objective function and constraint functions of NCI are related to l_e, N, g_s, and f_s. Consequently, the optimization process can focus solely on these four fundamental variables.

Because of the limited variability in number of N, the remaining three parameters are involved in the iteration under fixed N and efficiency constraint $\eta_{\lim}$ to obtain the optimal objective function. Subsequently, by iterating over both $\eta_{\lim}$ and N, the Pareto Front of the efficiency constraint and the objective function under various N can be obtained. The iteration range and parameters increment are presented in Table III.

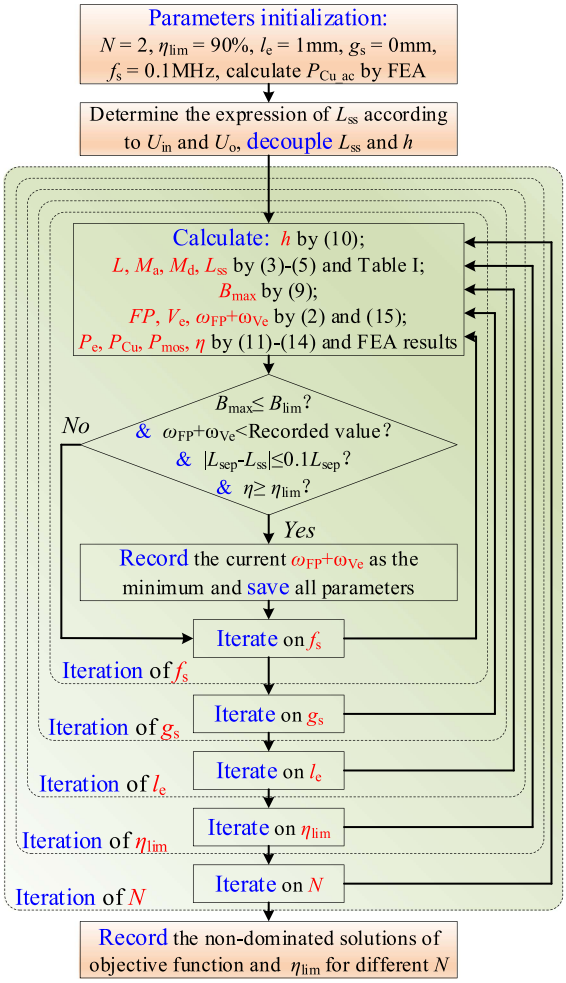

Fig. 12. Multiobjective optimization process for NCI.

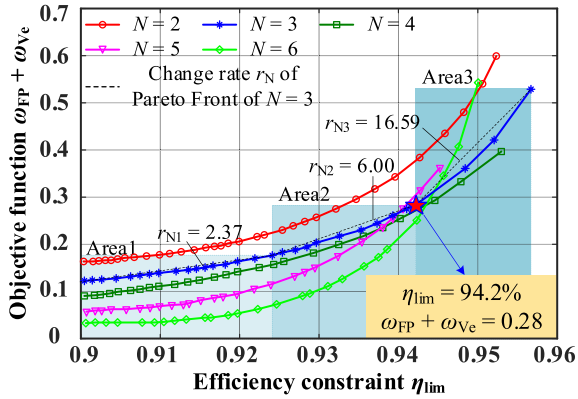

Fig. 13. Pareto Front of efficiency constraint and the objective function values under different winding turns.

The multiobjective optimization process for four-phase NCI in this article is illustrated in Fig. 12. The detailed procedures are outlined as follows.

Step 1: Initialization. Define the initial value for the fundamental parameters l_e, g_s, N, and f_s, initialize the recorded value of $\omega_{FP}+\omega_{Ve}$ to 0 under different values of N, and calculate P_{Cu_ac} under different variables using FEA.

Step 2: Decoupling. Based on the input and output voltages of the IBC, determine its steady-state duty cycle D. Referring to Table I, identify the equation for L_{ss} according to the range of D. By solving (4) and (10) simultaneously, decouple L_{ss} and h to derive their respective expressions.

Step 3: Calculation. Calculate h using its defined expression. Compute L, M_a, and M_d by (3) and (4), and calculate L_{ss} based on these results. Evaluate B_{max} using (9). Utilize (2) and (15) to calculate FP, V_e, and the objective function value $\omega_{FP\_j}+\omega_{Ve\_j}$. Assess core loss, winding loss, and MOSFET loss through (11)–(13) and FEA results, then finally compute the rated efficiency η of IBC based on these losses.

Step 4: Judgment. Verdict whether the computed values satisfy all constraints. If all constraints are satisfied, document the current $\omega_{FP\_j}+\omega_{Ve\_j}$ as the minimum of the objective function, then concurrently store all fundamental parameters before going to Step 5. If any parameter fails to meet the constraint requirements, proceed to Step 5 without altering the recorded value of the objective function.

Step 5: Iteration. Proceed parameter iteration on f_s, g_s, l_e, η_{lim}, and N in turn. Within the numerical range of each parameter, if the parameter in the current iteration loop is altered, all preceding iteration loops must be fully traversed.

Step 6: Recording. Document the nondominated solutions (Pareto Front) for η_{lim} and $\omega_{FP}+\omega_{Ve}$ under varying values of N.

By employing multiple iteration loops, the minimum of the objective function satisfying all constraints under different winding turns and efficiency constraint can be obtained.

B. Results of Multiobjective Optimization

After calculation, analysis, and recording, the Pareto Front of efficiency constraint and the objective function is divided according to the value of N, several curves representing Pareto Fronts under different N are presented in Fig. 13. From Fig. 13, it is evident that under the same η_{lim}, the value of $\omega_{FP}+\omega_{Ve}$ decreases as the value of N increases. Furthermore, the variation in the weighted value between $N = 3$ and $N = 4$ is less distinct compared to that between $N = 2$ and $N = 3$. Additionally, $N = 5$ and $N = 6$ do not lead to higher efficiency. Considering the complexity of PCB design and manufacturing cost, $N = 3$ is selected as the optimal choice.

Furthermore, as can be observed from Fig. 13, the variation curve for $N = 3$ is partitioned into three areas according to the regional change rate. It is evident that in Area3, the change rate of $\omega_{FP}+\omega_{Ve}$ with respect to η_{lim} increases significantly compared to the other two areas. By comprehensively evaluating the converter efficiency, as well as the NCI footprint and volume in this article, the design point corresponding to $\eta_{lim} = 94.2\%$ and $\omega_{FP}+\omega_{Ve} = 0.28$ is selected for the magnetic device designing. It can be seen from Fig. 13 that dividing the Pareto Front by the value of N avoids the problems of excessively high cost and design difficulties caused by too many winding turns, which makes the parameter tradeoff more intuitive.

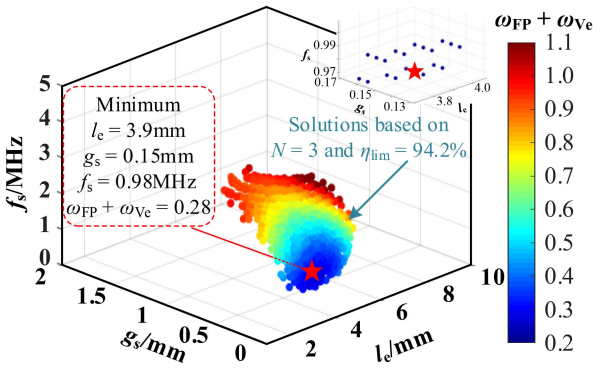

Fig. 14. Design results of weighted values under selected N and $\eta_{\lim}$.

TABLE IV
DESIGN RESULTS OF KEY PARAMETERS FOR NCI

Description	Parameter	Value
Number of turns	N	3
Column side length	l_e/mm	3.9
Air gap in column	g_s/mm	0.15
core window height	h_w/mm	2
Thickness of cover plates	h/mm	0.75
Switching frequency	f_s/MHz	0.98
Self-inductance	L/μH	3.25
Mutual-inductance	M_a/μH	-0.98
Mutual-inductance	M_d/μH	-0.91
equivalent steady-state inductance	L_{ss}/μH	2.17
Footprint of NCI	FP/mm^2	190.44
Volume of NCI	V_e/mm^3	666.54

Fig. 14 presents all design results regarding to $N = 3$ and $\eta_{\lim} = 94.2\%$, and the minimum point is indicated. Based on this point, the key parameters of the four-phase NCI are presented in Table IV.

Based on the aforementioned parameters in Table IV, a multiobjective optimized four-phase NCI model is structured. NCI is simulated using FEA, as illustrated in Fig. 15, the flux density distribution of NCI core at various time points depicted in Fig. 9 are relatively uniform and remain below 0.35T, satisfying both the design requirements and flux density constraint.

The multiphase NCI shown in Fig. 3 can also be optimized by employing the aforementioned multiobjective optimization method, according to the specific application of converter.

V. EXPERIMENTAL RESULTS AND ANALYSIS

As shown in Fig. 16, the designed four-phase NCI using the parameters obtained from the multiobjective optimization process and the designed EE-type magnetic core of SI based on the *AP* method are compared, while illustrating the winding distribution applied within the four-phase NCI.

In Fig. 16, the two magnetic devices exhibit identical maximum flux density and winding parameters. An air gap is located

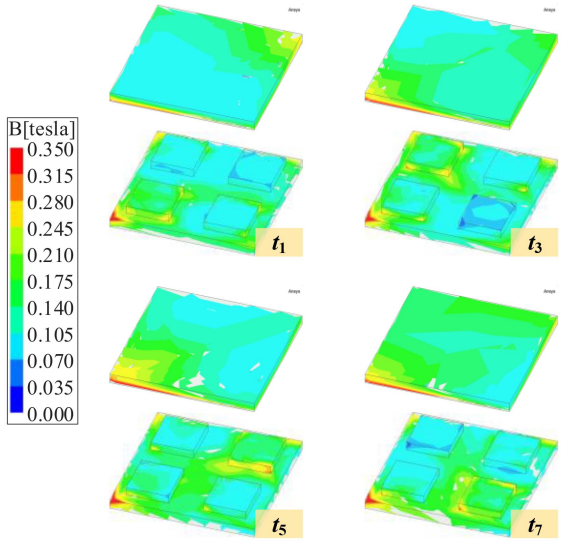

Fig. 15. FEA results of magnetic flux density in NCI at different times.

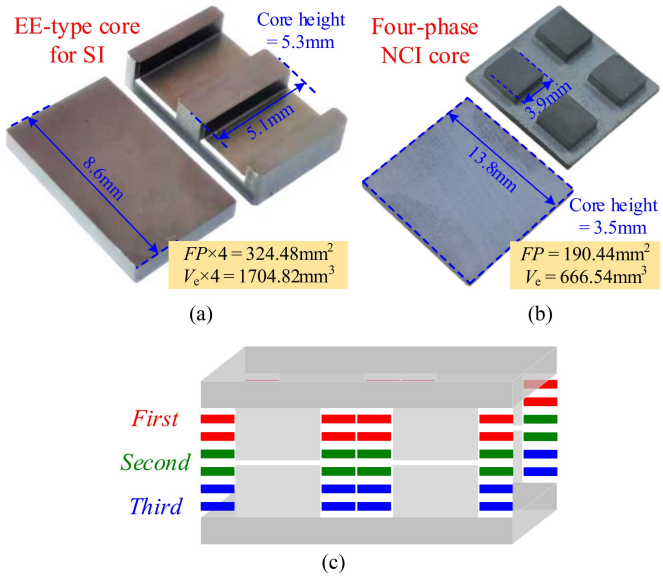

Fig. 16. SI and optimized NCI. (a) SI EE-type core. (b) Optimized NCI core. (c) Winding distribution applied within four-phase NCI.

in the core center column, with the $L_{\text{sep}} = 2.2$ μH for SI. By comparison, under identical operating conditions, the optimized four-phase NCI demonstrates a 41.31% reduction in footprint and a 60.90% reduction in volume. Furthermore, by applying the deduction process in Fig. 2 to SI core shown in Fig. 16(a), the four-phase NCI before optimization can be obtained, with a power density of 3633 W/in^3. After optimization, the power density of NCI achieves 7376 W/in^3, representing a 103.03% improvement compared to the unoptimized design, while satisfying the design requirements. These results validate the advantages of negative-coupling and the rationality of the multiobjective optimization.

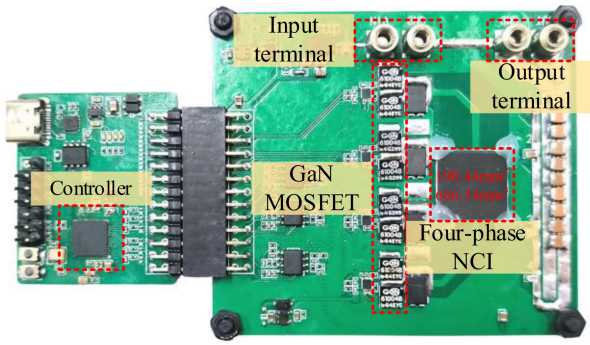

Fig. 17. Prototype of four-phase IBC.

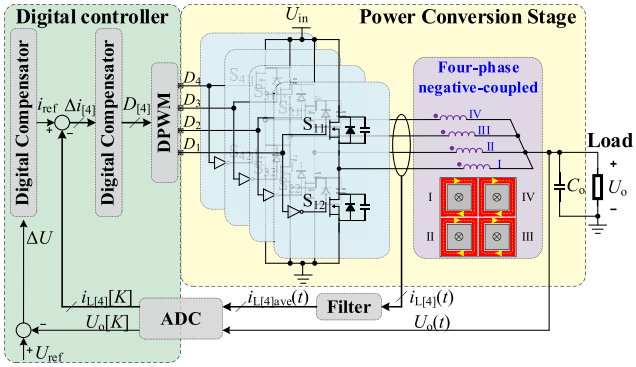

Fig. 18. Control flowchart of the four-phase IBC in this article.

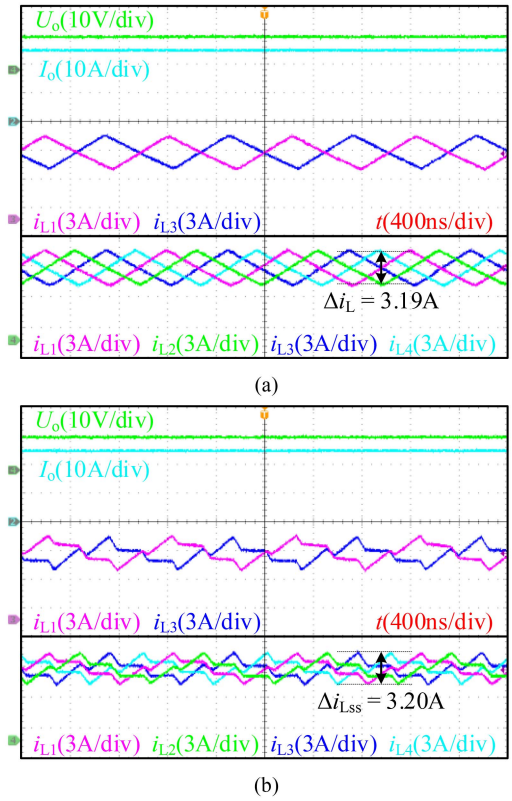

Fig. 19. Experimental waveforms of four-phase IBC at rated load power. (a) IBC with four-phase SI. (b) IBC with four-phase NCI.

TABLE V
PARAMETERS OF THE EXPERIMENTAL PLATFORM

Description	Parameter	Value
Input voltage	U_{in}/V	15–45 (rated value 28)
Output voltage	U_o/V	12
Rated output power	P_o/W	300
Switching frequency	f_s/MHz	0.5–2 (rated value 0.98)
Input filter capacitor	C_{in}/μF	200
Output filter capacitor	C_o/μF	250
MOSFET	\	GS61004B (V_{th} = 3.3 V)
Driver chip	\	LMG1205 (V_{gs} = 5 V)
Controller	\	TMS320F280049C

Based on the parameters provided in Table IV, a prototype experimental platform for a four-phase IBC is provided, as depicted in Fig. 17. And its control flow is shown in Fig. 18.

The parameters of the experimental platform are presented in Table V. Comparative experiments are performed on the two magnetic devices depicted in Fig. 16.

The experimental waveforms of the four-phase IBC at rated load power are shown in Fig. 19, which include output voltage, output current, and four-phase winding currents. As illustrated in Fig. 19, the four-phase winding currents operate with a phase increment of 90°. In Fig. 19(b), the winding current is segmented into 8 intervals due to the influence of negative-coupling, aligning with the configuration shown in Fig. 9. Moreover, the winding current ripple Δi_L and Δi_{Lss} in both Fig. 19(a) and (b) are measured at 3.19 A and 3.20 A, which not only corresponds to the parameter characteristics of the converter but also satisfies the design and optimization objectives of NCI.

Based on the parameters listed in Tables IV and V, supplementary experiments are carried out under two special conditions: the input voltage is adjusted to 21 V and the air gap is set to 0.6 mm. The corresponding waveforms are presented in Fig. 20. It is evident that when $U_{in} = 21$ V, the steady-state duty cycle D equals 0.57, and the four-phase current ripple remains identical to that observed at $U_{in} = 28$ V, which aligns with the descriptions provided in Fig. 10 and Table I. Furthermore, when the air gap g_s of NCI is set to 0.6 mm, L_{ss} is calculated as 1.18 μH, and the phase current ripple is measured as 6.00 A. Both aforementioned results are consistent with the theoretical calculations derived from (3)–(5) and Table I, as well as the description provided in Fig. 10.

It is important to note that, owing to the variation in g_s, the parameter characteristics of the NCI differ from those presented in Table IV. Consequently, the IBC cannot operate at the rated state, as doing so would lead to saturation of NCI core. Hence, the waveform depicted in Fig. 20(b) corresponds to the IBC operating under half-rated load. Fig. 20, thus, validates the correctness of the theoretical expressions and inferences related to the NCI.

As shown in Fig. 21, the transient experimental waveforms of IBC using two types of magnetic devices from half-rated load to rated load are presented. From the area marked by the dashed box

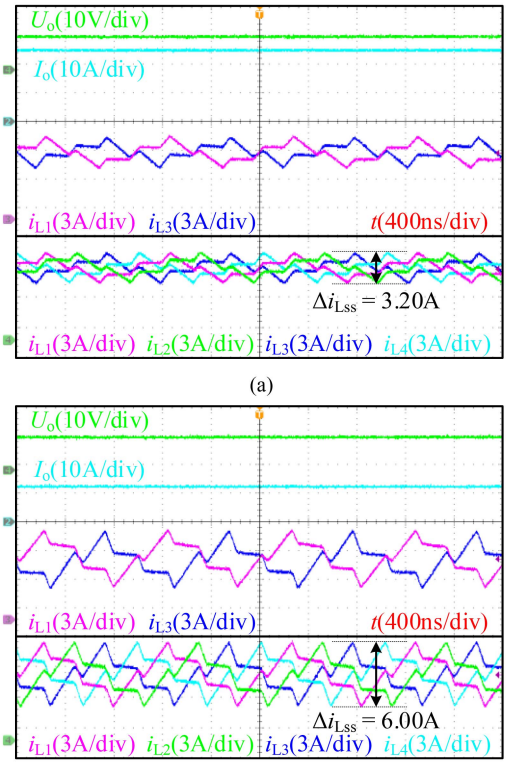

Fig. 20. Experimental waveforms of four-phase IBC under two special conditions. (a) $U_{\text{in}} = 21$ V. (b) $g_{\text{s}} = 0.6$ mm.

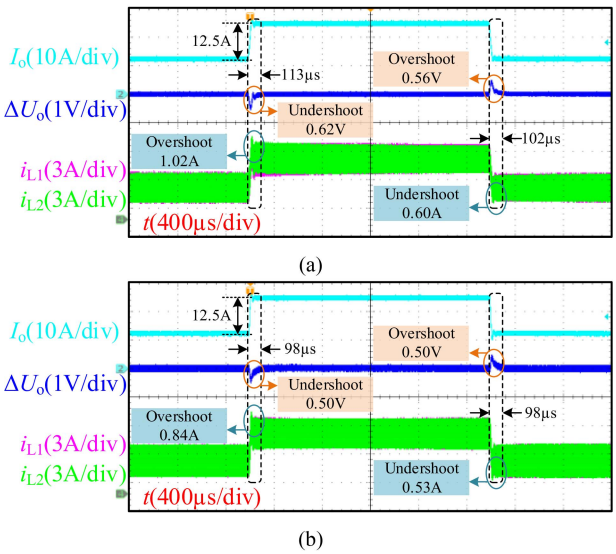

Fig. 21. Experimental waveforms of four-phase IBC utilizing two types of magnetic devices under transient load. (a) IBC using SI. (b) IBC using NCI.

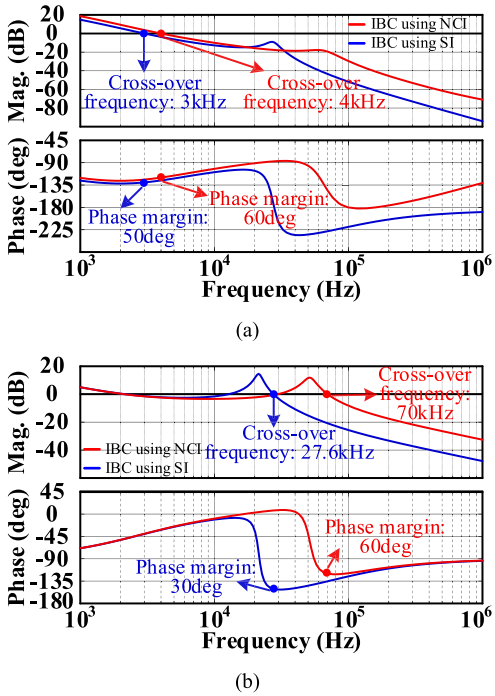

Fig. 22. Bode plots of the loop gain of IBC. (a) Voltage outer loop. (b) Current inner loop.

in figure, it can be observed that compared with SI, the IBC using NCI exhibits a faster regulation time and smaller overshoot and undershoot of output voltage and winding current during load transients, despite employing the same control strategy and control parameters. This is because negative-coupling effectively reduces the energy stored in the inductor, enhances the speed of energy transfer. Meanwhile, as shown in the Bode plots of the IBC loop gain in Fig. 22, compared with SI, the IBC using NCI has a larger voltage and current loop cross-over frequencies and phase margins. Therefore, negative-coupling optimizes the loop characteristics of the converter, thereby shortening the regulation time and reducing the overshoots and undershoots of voltage and current. In conclusion, Figs. 20 and 21 indicate that NCI is beneficial to improving the transient performance of the converter.

The efficiencies of the converter operating based on the parameters listed in Table V are measured when using two different magnetic devices, as depicted in Fig. 23. Fig. 23(a) shows the efficiencies at different f_{s} when $U_{\text{in}} = 28$ V, and Fig. 23(b) shows the efficiencies at different U_{in} when $f_{\text{s}} = 0.98$ MHz. The harmonic distribution of winding current in Fig. 19 is measured, as shown in Fig. 24.

As illustrated in Fig. 23(a), when the converter operates at $f_{\text{s}} = 0.98$ MHz, the rated efficiency of IBC using NCI achieves 1.45% higher than that obtained using SI, with measured values of 95.06% and 93.61%, respectively. Additionally, the rated efficiency of IBC with NCI satisfies the designed efficiency constraint $\eta_{\text{lim}} = 94.2\%$.

In addition, as shown in Fig. 23(a), the efficiency of IBC using optimized NCI is generally superior to that using SI with the EE-type core within full load range. Despite both having the similar winding current ripple, the root mean square value of the winding current in NCI is reduced due to the negative-coupling effect, thereby minimizing the associated loss. Moreover, under

TABLE VI
COMPARISON OF DESIGNED NCI WITH OTHER REFERENCES

References	NCI core structure	f_s	Num. of phases	Output power	Optimization method	Num. of optimization objectives	Converter efficiency at full load	Power density of NCI
[16]	Ladder core	103 kHz	3	30 kW	Pareto Front-based multi-objective optimization	2	98.00%	1244 W/in^3
[27]	PCB-embedded	20 MHz	4	12 W	Trade-off between NCI loss and footprint	2	95.00%	20802 W/in^3
[28]	Planar core with 5 columns	500 kHz	4	162 W	Optimization avoiding core saturation	1	84.22%	1529 W/in^3
[29]	Planar core with 4 columns	700 kHz	2	700 W	Tradeoff among 6 parameters	3	97.57%	2424 W/in^3
[30]	Planar core	30 kHz	2	50 kW	Design and optimization from experience	-	-	3472 W/in^3
[31]	EE-type core	2.2 MHz	2	3 kW	-	-	96.86%	2842 W/in^3
[32]	EE-type core	100 kHz	2	10 kW	Design and optimization using AP method	2	97.50%	529 W/in^3
[33]	EE-type core	100 kHz	2	400 W	Trade-off between Δi_L and coupling coefficient	2	96.41%	12.6 W/in^3
[34]	Ladder core	10 kHz	3	900 W	Pareto Front-based multi-objective optimization	2	-	1821 W/in^3
[35]	EE-type core	150 kHz	2	192 W	Pareto Front-based multi-objective optimization	2	90.27%	4189 W/in^3
article	Planar matrix core	980 kHz	4	300 W	Pareto Front-based multi-objective optimization	3	95.06%	7376 W/in^3

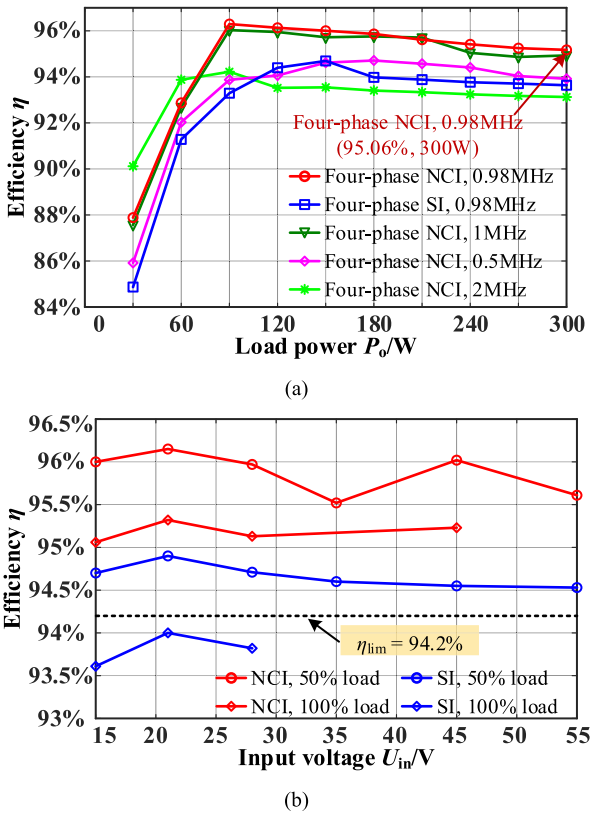

Fig. 23. Efficiencies of four-phase IBC. (a) Efficiencies at different f_s. (b) Efficiencies of 50% load and 100% load at different U_{in}.

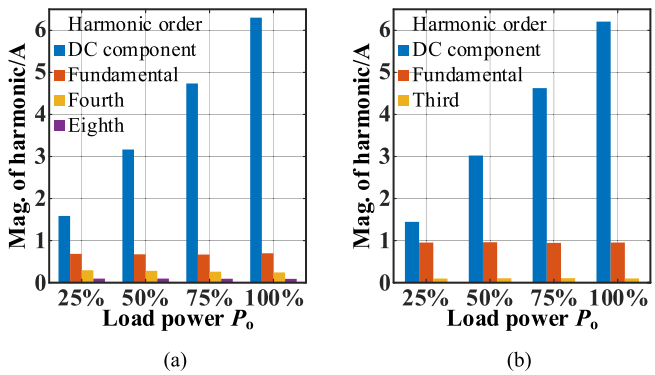

Fig. 24. Harmonic amplitudes of the NCI and SI winding current under different loads. (a) NCI current harmonics. (b) SI current harmonics.

the same flux density, NCI exhibits a smaller footprint and volume, leading to relatively lower core loss. In contrast, when $f_s = 0.5$ MHz, the larger winding current ripple results in higher loss. When $f_s = 1$ MHz and 2 MHz, the increase in switching loss reduces overall efficiency, thus validating the rationality of the multiobjective optimization.

From Fig. 23(b), it can be seen that when U_{in} is within the range of 15 V to 45 V, the rated efficiency of IBC using NCI all meets the constraint $\eta_{lim} = 94.2\%$. Whether at 50% load or 100% load, the efficiency of IBC using NCI is higher than that using SI. Moreover, the IBC using NCI can operate at $U_{in} = 45$ V (rated load) because the flux cancellation reduces the saturation of the core. Fig. 23(b) demonstrates the rationality of the multiobjective optimization method proposed in this article and indirectly indicates that compared with SI, NCI is beneficial for extending the U_{in} range of IBC to some extent.

In Fig. 24, whether using NCI or SI, the dc components in harmonic are similar. Although compared with SI, NCI increases the fourth and eighth harmonics due to four-phase negative coupling, it reduces fundamental harmonic and nearly eliminates the third harmonic. Therefore, NCI introduces no significant

changes in IBC core loss or electromagnetic noise, both remaining acceptable.

The comparison among this article and other relevant studies is presented in Table VI. By comparison, it can be concluded that the PCB-based planar matrix NCI core designed in this article has more advantages in reducing magnetic volume and improving integration with the converter. Through normalization and weighting of the optimization objectives (FP and V_e) in the Pareto Front-based multiobjective optimization, simultaneous optimization of NCI footprint, volume, and IBC efficiency is achieved, leading to high NCI power density and acceptable IBC efficiency. In comparison, the NCI in this article has higher power density, it actually demonstrates the practicality of NCI structure design, the accuracy of mathematical modeling, and the practicality of the multiobjective optimization method in this article to some extent. Although compared to [27], the power density of the NCI in this article is lower, it has advantages in terms of power and switching frequency. And the full-load efficiency of the converter in this article remains comparable as those in other works. Considering a larger $\eta_{\lim}$ in the parameter tradeoff can improve the converter efficiency, but at the expense of the NCI optimization.

In general, Figs. 16–24 and Table VI present a comprehensive evaluation of the optimization for magnetic devices in terms of footprint, volume, and converter efficiency through comparative analysis and experiments. They demonstrate that the multiobjective optimization successfully fulfills the design objectives of four-phase NCI. Furthermore, these figures and table not only emphasize the superiority of NCI over SI regarding footprint, volume, efficiency, and power density, but also confirm the validity of the optimized four-phase NCI structure as well as the feasibility of the proposed mathematical modeling and multiobjective optimization methods.

VI. Conclusion

To simultaneously optimize the converter efficiency, the footprint and volume of magnetic device, this article proposes a comprehensive mathematical modeling and multiobjective optimization method for multiphase NCI in interleaved dc–dc converter, and concentrates on the specific content by taking four-phase NCI and IBC as an example. A novel four-phase NCI without core center column is designed utilizing flux cancellation. Based on the NCI and IBC, mathematical models are established regarding essential parameters to accurately describe their characteristics. A multiobjective optimization process based on modeling results is employed to obtain the Pareto Front of efficiency constraint and objective function. Referring to the optimization results, NCI is manufactured according to optimal parameters. Compared with SI, the designed NCI reduces footprint by 41.31% and volume by 60.90%, achieving a power density of 7376 W/in^3 after optimization. A 300 W IBC prototype is used for comparative experiments, showing that IBC using NCI has 1.45% higher rated efficiency and better transient performance than using SI, while satisfying the design requirements. The research provides valuable guidance for designing multiphase coupled inductor and related converters.

Acknowledgment

The author would like to thank Southwest Institute of Applied Magnetism, China Electronics Technology Group Corporation for providing high-frequency magnetic cores for the research in this article.

References

[1] J. T. Boys, G. A. J. Elliott, and G. A. Covic, "An appropriate magnetic coupling co-efficient for the design and comparison of ICPT pickups," *IEEE Trans. Power Electron.*, vol. 21, no. 1, pp. 333–335, Jan. 2007.

[2] N. Swaminathan and Y. Cao, "An overview of high-conversion high-voltage DC-DC converters for electrified aviation power distribution system," *IEEE Trans. Transp. Electrific.*, vol. 6, no. 4, pp. 1740–1754, Dec. 2020.

[3] Y. Wei, Q. Luo, and A. Mantooth, "Overview of modulation strategies for LLC resonant converter," *IEEE Trans. Power Electron.*, vol. 35, no. 10, pp. 10423–10443, Oct. 2020.

[4] F. C. Lee, Q. Li, and A. Nabih, "High frequency resonant converters: An overview on the magnetic design and control methods," *IEEE J. Emerg. Sel. Topics Power Electron.*, vol. 9, no. 1, pp. 11–23, Feb. 2021.

[5] F. C. Lee, S. Wang, and Q. Li, "Next generation of power supplies-design for manufacturability," *IEEE J. Emerg. Sel. Topics Power Electron.*, vol. 9, no. 6, pp. 6462–6475, Dec. 2021.

[6] M. Li, C. Wang, Z. Ouyang, and M. A. E. Andersen, "Optimal design of a matrix planar transformer in an LLC resonant converter for data center applications," *IEEE J. Emerg. Sel. Topics Power Electron.*, vol. 11, no. 2, pp. 1778–1787, Apr. 2023.

[7] C. Zhou, F. Zhang, C. Xu, and T. Tu, "Improvement of planar integrated matrix transformer for CM noise cancellation applied to full-bridge LLC-DCX converter," *IEEE Trans. Power Electron.*, vol. 39, no. 10, pp. 13134–13145, Oct. 2024.

[8] Y. Liu, H. Wu, S. Ni, Y. Song, and F. Yang, "Lower-height-oriented magnetic integration design for onboard power converter of electric vehicles," *IEEE Trans. Transp. Electrific.*, vol. 10, no. 1, pp. 163–173, Mar. 2024.

[9] X. Ma, P. Wang, Y. Wang, L. Tao, and P. Cheng, "Penalty and barrier-based numerical optimization for efficiency and power density of interleaved buck-boost converter," *IEEE Trans. Power Electron.*, vol. 37, no. 10, pp. 12095–12107, Oct. 2022.

[10] N. Naseem and H. Cha, "Triple-active-bridge converter with automatic voltage balancing for bipolar DC distribution," *IEEE Trans. Power Electron.*, vol. 37, no. 7, pp. 8640–8648, Jul. 2022.

[11] Z. Cao et al., "A low loss orthogonal decoupling magnetic integrated structure for dual active bridge converter," *IEEE Trans. Power Electron.*, vol. 37, no. 6, pp. 7013–7027, Jun. 2022.

[12] S. Wang, P. H. Pham, Q. Li, A. Nabih, and P. R. Prakash, "PCB winding-based coupled inductor for a high-frequency DC/DC converter with 99% efficiency," in *Proc. IEEE Appl. Power Electron. Conf. Expo.*, 2023, pp. 420–425.

[13] H. Zhu, D. Zhang, Y. Zhou, C. Zhang, and Y. Zhang, "Integrated magnetic buck-boost converter with 'zero' output current ripple," *IEEE Trans. Ind. Electron.*, vol. 68, no. 7, pp. 5821–5832, Jul. 2021.

[14] S. Wang, F. C. Lee, and Q. Li, "Improved balance technique for common-mode noise suppression of PCB-based PFC," *IEEE Trans. Power Electron.*, vol. 37, no. 4, pp. 4174–4182, Apr. 2022.

[15] Z. Huang, G. Son, Q. Li, and F. C. Lee, "Balance techniques and PCB winding magnetics for common-mode EMI noise reduction in three-phase AC-DC converters," *IEEE Trans. Power Electron.*, vol. 37, no. 3, pp. 3130–3142, Mar. 2022.

[16] Y. Wang, Z. Wang, X. Ma, H. Cui, J. Zhou, and H. Shi, "Genetic algorithm-based multi-objective optimization of three-phase coupled inductor with ladder magnetic core," *IEEE J. Emerg. Sel. Topics Power Electron.*, vol. 13, no. 4, pp. 5363–5376, Aug. 2025.

[17] F. Zhu and Q. Li, "Coupled inductors with an adaptive coupling coefficient for multiphase voltage regulators," *IEEE Trans. Power Electron.*, vol. 38, no. 1, pp. 739–749, Jan. 2023.

[18] O. C. D. S. Filho, F. L. Tofoli, P. Zacharias, and D. D. S. Oliveira, "Magnetic integration in high-frequency-isolated AC-AC interleaved converters," *IEEE J. Emerg. Sel. Topics Power Electron.*, vol. 11, no. 4, pp. 4199–4211, Aug. 2023.

[19] C. Fei, F. C. Lee, and Q. Li, "High-efficiency high-power-density LLC converter with an integrated planar matrix transformer for high-output current applications," *IEEE Trans. Ind. Electron.*, vol. 64, no. 11, pp. 9072–9082, Nov. 2017.

[20] R. Gadelrab and F. C. Lee, "PCB-based magnetic integration and design optimization for three-phase LLC," *IEEE Trans. Power Electron.*, vol. 38, no. 11, pp. 14037–14049, Nov. 2023.
[21] X. Chen, G. Xu, Q. Shen, Y. Sun, and M. Su, "Magnetizing and leakage inductance integration for split transformers with standard UI cores," *IEEE Trans. Power Electron.*, vol. 37, no. 11, pp. 12980–12985, Nov. 2022.
[22] A. Stratta et al., "Optimal integrated design of a magnetically coupled interleaved H-bridge," *IEEE Trans. Power Electron.*, vol. 37, no. 1, pp. 724–737, Jan. 2022.
[23] Z. Li, E. Hsieh, Q. Li, and F. C. Lee, "High-frequency transformer design with medium-voltage insulation for resonant converter in solid-state transformer," *IEEE Trans. Power Electron.*, vol. 38, no. 8, pp. 9917–9932, Aug. 2023.
[24] S. Kimura, Y. Itoh, W. Martinez, M. Yamamoto, and J. Imaoka, "Downsizing effects of integrated magnetic components in high power density DC-DC converters for EV and HEV applications," *IEEE Trans. Ind. Electron.*, vol. 52, no. 4, pp. 3294–3305, Jul./Aug. 2016.
[25] Y. Duo, Z. Ouyang, and M. A. E. Andersen, "Integrated coupled inductors with functionality of current balancing transformer for two-phase synchronous DC-DC converters," *IEEE Trans. Power Electron.*, vol. 35, no. 5, pp. 4472–4476, May 2020.
[26] C. Fei, Y. Yang, Q. Li, and F. C. Lee, "Shielding technique for planar matrix transformers to suppress common-mode EMI noise and improve efficiency," *IEEE Trans. Ind. Electron.*, vol. 65, no. 2, pp. 1263–1272, Feb. 2018.
[27] F. Zhu and Q. Li, "A novel PCB-embedded coupled inductor structure for a 20-MHz integrated voltage regulator," *IEEE J. Emerg. Sel. Topics Power Electron.*, vol. 10, no. 6, pp. 7452–7463, Dec. 2022.
[28] F. Zhu, X. Lou, and Q. Li, "An improved hybrid-coupled inductor structure with flux reduction and integrated controllable coupling function," *IEEE Trans. Power Electron.*, vol. 39, no. 1, pp. 1103–1114, Jan. 2024.
[29] Y. Liu et al., "Optimized air-gap configuration for an integrated coupled inductor with lower height and reduced core/winding losses," *IEEE Trans. Ind. Appl.*, vol. 60, no. 2, pp. 2980–2990, Mar./Apr. 2024.
[30] Y. Cao et al., "Common-mode noise reduction and capacitor voltage autobalance using bridged midpoints and coupled inductor in a 3-L buck-boost converter," *IEEE Trans. Power Electron.*, vol. 38, no. 10, pp. 12365–12369, Oct. 2023.
[31] M. Chen et al., "A coupled inductor scheme for CLLC bidirectional converter and optimized current detection method," *IEEE Trans. Power Electron.*, vol. 37, no. 10, pp. 11546–11551, Oct. 2022.
[32] Z. Wang, C. Li, Z. Zheng, H. Jiang, and Z. Huang, "A DC flux cancellation design method for inverse-coupled inductors used in interleaved boost converters," *IEEE Trans. Transp. Electrific.*, vol. 10, no. 2, pp. 2956–2964, Jun. 2024.
[33] N. Surulivel, D. Debnath, and C. Chakraborty, "A novel single coupled-inductor boost TPC with two inductively interfaced ports suitable for renewable energy integration," *IEEE Trans. Ind. Electron.*, vol. 70, no. 5, pp. 4705–4715, May 2023.
[34] T. Kang, A. Gandomkar, J. Lee, and Y. Suh, "Design of optimized coupling factor for minimum inductor current ripple in DC-DC converter using multiwinding coupled inductor," *IEEE Trans. Ind. Appl.*, vol. 57, no. 4, pp. 3978–3989, Jul./Aug. 2021.
[35] Z. Dang and J. A. A. Qahouq, "Permanent-magnet coupled power inductor for multiphase DC-DC power converters," *IEEE Trans. Ind. Electron.*, vol. 64, no. 3, pp. 1971–1981, Mar. 2017.

Ze Liu received the B.S. degree in electrical engineering and automation from Shaanxi University of Science and Technology, Xi'an, China, in 2022. He is currently working toward the Ph.D. degree in electrical engineering with Southwest Jiaotong University, Chengdu, China.

His research interests include magnetic integration technology, control strategies for high-frequency converters and high-efficiency dc–dc converter topologies.

Guohua Zhou (Senior Member, IEEE) received the B.S. degree in electronic and information engineering and the M.S. and Ph.D. degrees in electrical engineering from Southwest Jiaotong University, Chengdu, China, in 2005, 2008, and 2011, respectively.

From Mar. 2010 to Sep. 2010, he was a Research Assistant with the Department of Electronic and Information Engineering, Hong Kong Polytechnic University, Kowloon, Hong Kong. From 2010 to 2011, he was a Visiting Scholar (also a Joint Ph.D. student) with the Center for Power Electronics Systems, Virginia Polytechnic Institute and State University, Blacksburg, VA, USA. He is currently a Professor with the School of Electrical Engineering, Southwest Jiaotong University. His current research interests include modulation and control techniques of power electronics systems, modeling and stability analysis of switching power converters, and renewable energy applications of power electronics.

Dr. Zhou was the recipient of the National Excellent Doctoral Dissertation of China in 2014. He was elected as a Fellow of the Institution of Engineering and Technology in 2018. He is currently an Associate Editor of CPSS Transactions on Power Electronics and Applications.

Yingjie He was born in Sichuan Province, China, in 2001. He received the B.S. degree in microelectronic science and engineering from Chengdu Technological University, Chengdu, China, in 2023. He is currently working toward the M.S. degree in electrical engineering with Southwest Jiaotong University, Chengdu, China.

His research interests include high-efficiency dc–dc converter topologies and control strategies, as well as modulation and control strategies for pulsewidth modulation rectifiers.

Nengmou Xu (Student Member, IEEE) received the B.S. degree in electrical engineering and automation from Qinghai University, Xining, China, in 2019. He is currently working toward the Ph.D. degree in electrical engineering with Southwest Jiaotong University, Chengdu, China.

His research interests include multilevel inverter topologies, multiport power converter and its control strategies for renewable energy and energy storage systems.